Photometry from Voyager 2: Initial Results from the Uranian Atmosphere, Satellites, and Rings

Arthur L. Lane, Charles W. Hord, Robert A. West, Larry W. Esposito, Karen E. Simmons, Robert M. Nelson, Brad D. Wallis, Bonnie J. Buratti, Linda J. Horn, Amara L. Graps, Wayne R. Pryor

The Voyager 2 photopolarimeter successfully completed the Uranus encounter, acquiring new data on the planet's atmosphere, its principal satellites, and its ring system. Spatially resolved photometry of the atmosphere at 0.27 micrometer shows no enhancement in absorption toward the pole, unlike the case for Jupiter and Saturn. Stellar occultation measurements indicate the temperature at the 1-millibar level over the north pole is near 90 kelvins. The geometric albedos of the five large satellites of Uranus were measured at 0.27 and 0.75 micrometer and indicate the presence of low albedo, spectrally flat absorbing material. Titania seems to have a fluffy surface, as indicated by its phase curve. The nine ground-based rings were detected, and their internal structure, optical depths, and positions were determined. The sharp edges of the ε ring made it possible to measure its edge thickness (less than 150 meters) and particle sizes (less than 30 meters); little or no dust was detected. New narrow rings and partial rings (arcs) were measured, and the narrow component of the η ring was found to be discontinuous.

The encounter strategy for the photopolarimeter (PPS) on Voyager 2 during its flyby of Uranus was considerably more ambitious than the strategy implemented at Saturn (*1*), even considering the smaller time window available to accomplish its scientific goals. During Voyager's cruise between Saturn and Uranus, the PPS was recalibrated and its photometric behavior refined; this led to photometry measurements with better than 2% reproducibility. The stars selected for ring occultation, σ Sagittarii and β Persei (Algol), were examined for temporal stability. The eclipse light curve of β Persei was found to be stable at phase 0.766 for the Uranus occultation event. The PPS completed its cruise-phase testing with no changes from its performance during the Saturn encounter and achieved its planned measurements in the Uranus system. We now describe initial results from (i) the Uranus atmospheric scattering and occultation measurements, (ii) the two stellar occultations of the Uranian ring system, and (iii) measurements of the geometric albedos of the satellites and the phase curve of Titania.

Atmospheric scattering and occultation measurements. The objectives for the atmospheric measurements were to obtain photometry and polarimetry data at various emission and phase angles in two channels whose solar-flux weighted effective wavelengths are 0.27 and 0.75 μm. The value of 0.27 μm for the ultraviolet (UV) filter differs from the effective wavelength reported earlier (0.264 μm) because the wavelength calibration for that filter was revised (*1*). In the absence of aerosols, unit optical depth for the UV channel occurs around 0.2 bar (assuming 85% H_2 and 15% He). The UV channel is insensitive to cloud structure at pressures greater than about 1 bar. Additional objectives were to measure the occultation light curve of γ Pegasi by the Uranian atmosphere to obtain a temperature at pressures around 1 mbar near the north (dark) pole, and to search for aerosol layers at pressures lower than 10 mbar.

We obtained raster scan maps of the illuminated disk as well as individual scans across the disk. A circular field of view 0°.12 in diameter was used for these measurements. The maps were obtained at relatively low phase angles (16° to 30°). Higher phase angle measurements, mostly between −20° and −30° latitude, were also acquired. The magnitude and sign of the polarization near a phase angle of 110° are consistent with scattering by molecules or very small particles, but they require an aerosol component having less polarization in the infrared.

The raster scan map of the south pole shown in Fig. 1 was obtained 1.7×10^6 km from Uranus center, when the phase angle was nearly 17°. The amount of UV absorption and its latitudinal distribution on Uranus are strikingly dissimilar to the amounts and distributions reported earlier for Jupiter or Saturn (*1, 2*). The larger Jovian planets have a strong UV absorption that increases from equator to pole; the much weaker UV absorption on Uranus does not show enhancement at the pole at 0.27 μm. The absorption in the middle UV range indicates the presence of molecules more complex than those measured by the Voyager IRIS and UVS. Polymerized acetylene is a possible UV-absorbing aerosol (*3*).

For quantitative modeling, we chose a single slow scan across the disk that starts near the bright limb, passes over the pole, and continues to the terminator (phase angle ~ 21°). These data were obtained at a distance of 0.9×10^6 km and have higher spatial resolution than the map data in Fig. 1.

Figure 2 shows a comparison of observations and three homogeneous models (solid curves) that differ only in the effective single-scattering albedo ($\tilde{\omega}_0$) of the gas absorb-

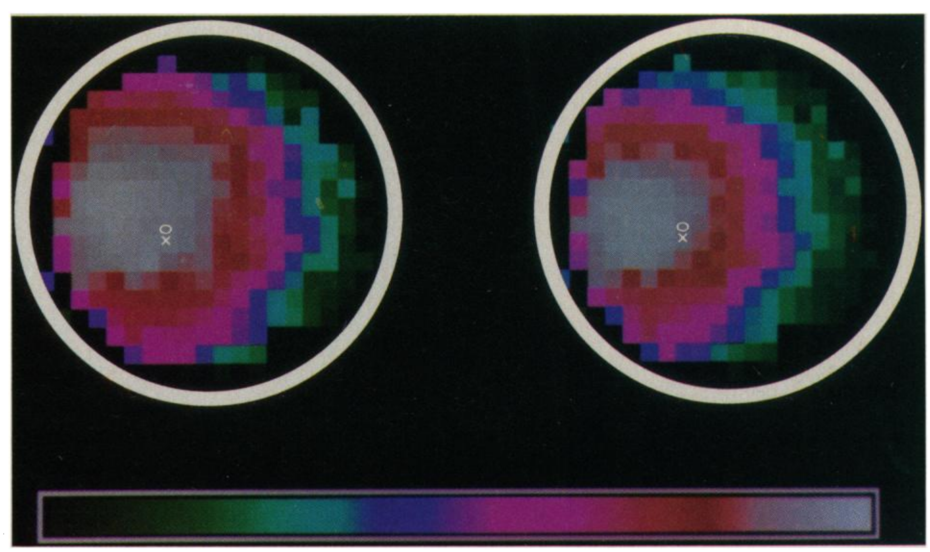

Fig. 1. False-color images of Uranus at 0.27 μm (left) and 0.75 μm (right). The maximum intensities are gray in these representations and correspond to *I*/*F* (*I*, observed intensity; π*F*, incident solar flux) of 0.48 in the UV and 0.30 in the IR. The south pole is slightly offset to the left of center of the disk. The spin axis (south pole) is shown by the cross and the subsolar point by the circle.

A. L. Lane, R. A. West, R. M. Nelson, B. D. Wallis, B. J. Buratti, L. J. Horn, Jet Propulsion Laboratory, California Institute of Technology, Pasadena, CA 91109.
C. W. Hord, L. W. Esposito, K. E. Simmons, A. L. Graps, W. R. Pryor, Laboratory for Atmospheric and Space Physics, University of Colorado, Boulder, CO 80309.

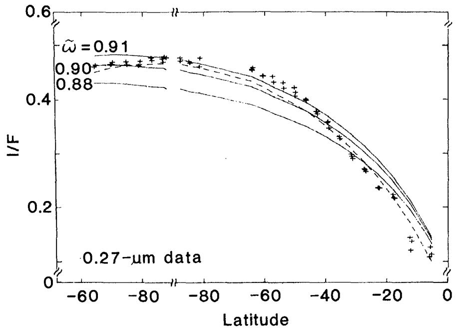

Fig. 2. Observed reflectivity at 0.27 μm (+) from a scan across the illuminated disk of Uranus from near the bright limb (left) to near the terminator (right). The solid curves represent three homogeneous gas-plus-absorber models whose effective single-scattering albedos are labeled; the dashed curve represents a vertically inhomogeneous model that has UV absorbers concentrated in the upper 0.1 optical depth.

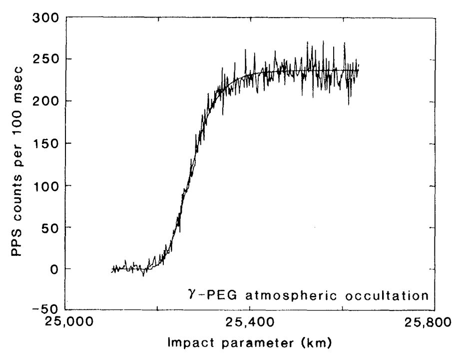

Fig. 3. The egress occultation light curve of γ Pegasi (γ-PEG) binned in ten 10-msec samples (minus background) plotted as a function of impact parameter (the radial distance of the line-of-sight tangency point on a sky projection of the planet). The abscissa coordinate is an estimate based on pre-Voyager estimates of the polar radius. Also shown is a smooth curve derived from a least-squares solution to the temperature profile, whose values at 10, 1, and 0.1 mbar are, respectively, 86, 90, and 97 K. Only the temperature at 1 mbar is well constrained.

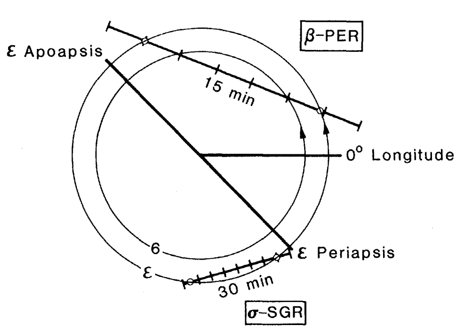

Fig. 4. Occultation geometries. The first occultation with σ Sagittarii (σ-SGR) passed behind the ε and δ rings in a nearly tangential occultation as viewed from Voyager as it approached Uranus. The second occultation with β Persei (β-PER) cut radially across all the known rings while the star was viewed from behind the planet. Every 10 msec the PPS recorded the brightness of the occulted star, with successive data points separated by 10 m (σ-SGR) or 100 m (β-PER) in distance from Uranus' center. The periapse and apoapse of the highly eccentric ε ring are shown relative to the two occultation paths.

er mix. The calculations were carried out with a vector doubling-adding code that accounts for linear polarization (*4*), an important effect in the UV (*5*). We calculated a Raman effective single-scattering albedo (*5*) of 0.992, which approximately accounts for the net loss of photons from our UV channel as a result of Raman scattering. Only the difference between this value and $\tilde{\omega}_0$ is due to UV absorbers.

A single homogeneous model cannot fit all latitudes. Either the effective single-scattering albedo decreases (that is, the concentration of absorbers increases) toward the equator or another type of structure describes the distribution of absorbers. A modification whereby the upper 0.1 optical depth has $\tilde{\omega}_0 = 0.4$ and the deeper atmosphere has $\tilde{\omega}_0 = 0.93$ comes close to fitting the data. The remaining residuals may be due to pointing errors, latitudinal structure, or incorrect vertical structure. Additional constraints from data at other phase angles will help to disentangle these possible contributions.

Discrete aerosol layers at pressures lower than about 10 mbar are ruled out by the occultation egress light curve of γ Pegasi (Fig. 3). A uniformly mixed aerosol could not be detected from a cursory inspection but may well be present. The data are binned in ten 10-msec samples, providing sampling intervals of 1.8 km in altitude.

We solved for a best-fit temperature profile on the assumption that aerosols do not contribute. Extinction by molecular scattering, rather than refraction, dominates the flux loss along the ray path. The half-power point occurs near the 1-mbar ray tangent for 0.27-μm photons; that is the level where our derived temperature is most certain. We find $T(1 \text{ mbar}) = (90 \pm 2) \cdot (\mu/2.3)$, where T is temperature (in kelvins) and μ is the mean molecular weight of the atmosphere. The best-fit values at 10 and 0.1 mbar are 86 K and 97 K, respectively, but their uncertainties are very large since the signal is nearly 0 at 10 mbar and nearly at its free-space value at 0.1 mbar. A more careful study will be performed to infer tempera-

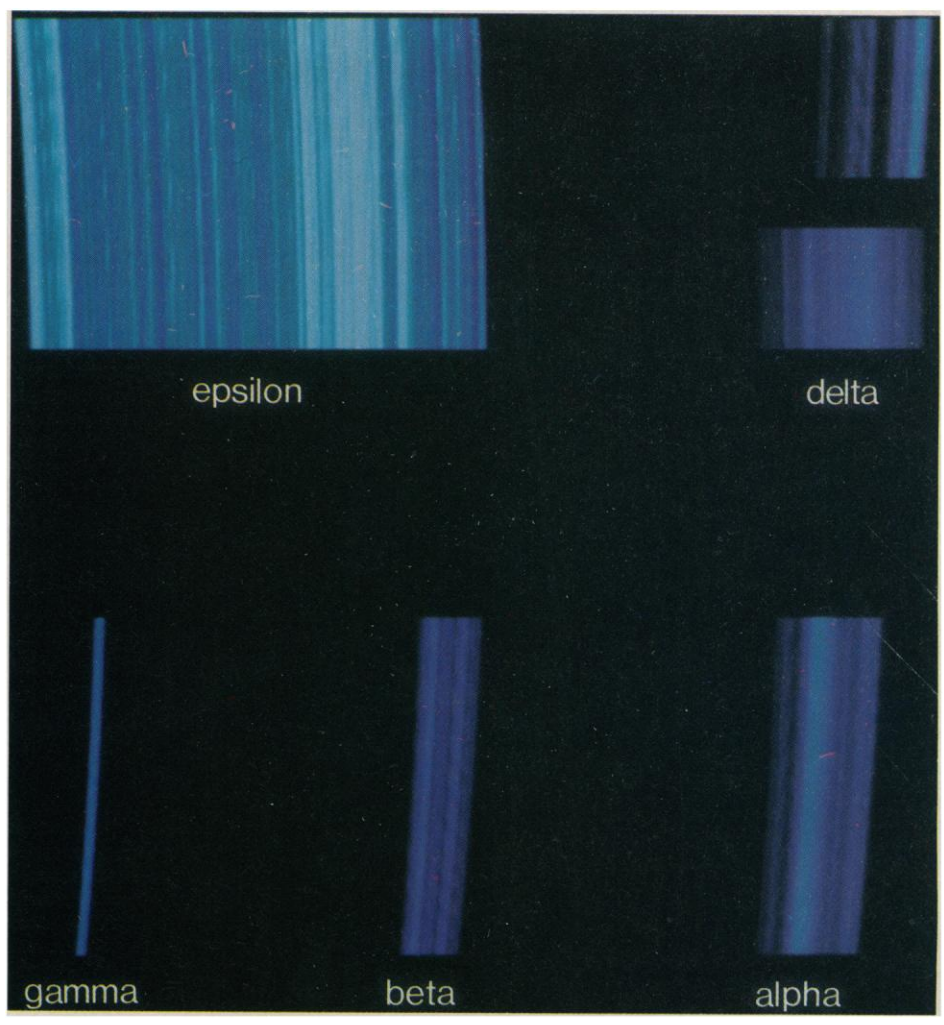

Fig. 5. The five most opaque rings of Uranus as seen by the Voyager PPS occultation. The data for the ε ring were smoothed to 100-m resolution. For the other rings, data were smoothed to 1-km resolution. This image was created from individual cuts across each of the rings on the assumption of azimuthal symmetry.

tures one scale-height above and below the half-power point and to address the issue of pole-to-equator temperature differences if the temperature at 1 mbar near the equator can be obtained from the radio occultation measurements (*6*).

Stellar occultations by the Uranian ring system. On 24 January 1986 universal time (U.T.) the Voyager 2 PPS performed two Uranian ring occultation experiments. For each occultation, 0.27-μm UV-filtered light from the selected star was sampled 100 times per second (*1, 7*) while the star was in the vicinity of the previously known nine rings (*8*). Each occultation geometry was unique (Fig. 4). Because on both ingress and egress each star was blocked by the rings, we obtained four profiles of the ε and δ rings and two profiles of each of the other rings. These occultation paths provided data for questions concerning the orientation, eccentricities, and inclinations of the rings. It also raised the question of the azimuthal continuity of the individual rings.

Table 1 lists characteristics of the nine previously known Uranian rings, the newly discovered ring 1986U1R (*9*), and several new features in the PPS data. For ease of presentation, we have converted subsets of our data into two-dimensional images on the assumption of azimuthal symmetry in the rings (Fig. 5). These images represent false-color pictures of what an observer or camera might see from a point where the resolution is the same as that provided by the PPS stellar occultation.

Our profiles confirm the broad structure seen from Earth (*8*) at low resolution. At higher resolution, we see a multitude of new structure. Comparison of ingress and egress data for the ε ring, for example (Fig. 6), shows that the new features are real, although the exact shape and relative opacity varies with longitude. By comparing the ε ring's mean optical depth observed by the PPS at the four longitudes sampled by the stellar occultations, we determine that the total amount of material is constant to approximately 10%, even though the measured width varies from 20 to 90 km. For several of the other rings, the variability of material with longitude is much greater. Our results also agree with ground-based observations (*8*) if their inferred optical depths are divided by 2 to allow for diffraction (*10*).

The edges of the ε and γ rings are sharp. At the outer edge of the ε ring, the counting rate makes the transition from its free-space value to nearly 0 in a radial distance of less than 40 m. The inner edge shows this same transition in about 500 m. Because the line of sight from the PPS to these stars is not perpendicular to the ring plane, the ray from the star at any instant samples material at different radii from Uranus. The sharpness of the transition from opaque to transparent thus provides an upper limit to the vertical extent of the ring at that edge (*1*). We find an upper limit on the vertical extent of about 150 m or less at the ε ring's outer edge. Because our measured optical depth in the ε

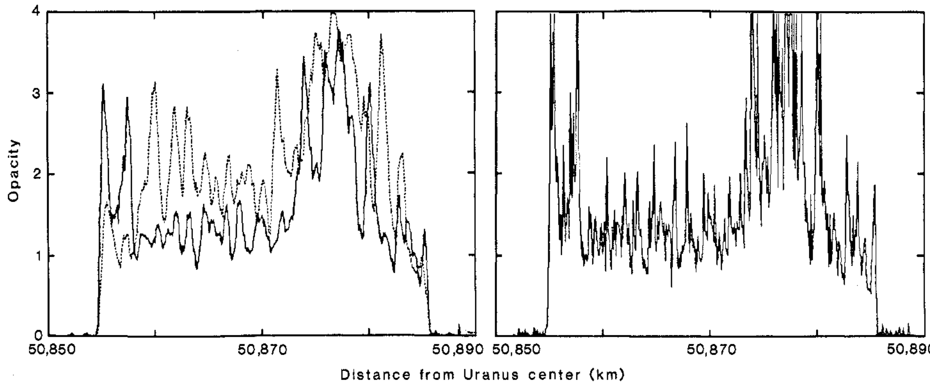

Fig. 6 (left). The ε ring as seen during the ingress (solid line) and egress (broken line) of the σ Sagittarii occultation. The data are smoothed to a resolution of approximately 500 m and have been corrected for the variation of the ring width due to its ellipticity. The range shown is appropriate for the ingress data set and does not apply to the geometrically transformed egress set. At this resolution, nearly all features are seen in both data sets, although the relative opacity varies. Fig. 7 (right). Features in the ε ring that resemble density-wave crests seen in Saturn's rings: they are sharp, narrow, and separated by broad troughs. The data are from the σ Sagittarii ingress and are smoothed to 100-m resolution.

Table 1. Characteristics of the Uranian rings.

Ring	Star and path*	Midpoint range† (km)	Width‡ (km)	Longitude (deg)	Mean optical depth§	Comments
			Previously known rings			
ε	SSI	50,870	30	267	1.6	$\tau_{max} \geq 4.0$
	SSE	50,750	22	306	2.1	
	BPI	50,990	41	22	1.4	$\tau_{max} \geq 2.8$
	BPE	51,540	93	116	0.5 ± 0.05	
1986U1R	SSI	50,030	2		0.09 ± 0.02	
	SSE	50,030	1		0.12 ± 0.02	
δ	SSI	48,310	7	279	0.4	
	SSE	48,310	7	294	0.4	
	BPI	48,310	9	25	0.3	Three components
	BPE	48,310	7	113	0.3	Diffuse region just inside ring
γ	BPI	47,630	1	26	2.3 ± 1.0	$\tau_{max} \geq 2.8$
	BPE	47,630	3	112	1.3	
η	BPI				~0.1	Upper limit only
	BPE	47,180	2	111	0.4	Narrow component clearly seen on egress only
β	BPI	45,660	8	29	0.2	
	BPE	45,690	11	109	0.2	
α	BPI	44,760	11	30	0.3	
	BPE	44,750	7	107	0.4	
4	BPI	42,600	2	34	0.3	
	BPE	42,610	2	104	0.3	Opacity peaks at outer edge
5	BPI	42,320	2	35	0.5	
	BPE	42,240	2	103	0.6	
6	BPI	41,880	3	36	0.2	
	BPE	41,830	1	102	0.3	
			New ring features			
Ring 1	BPI	50,660	16		0.1	>5σ detection
	BPE	50,670	16		0.1	
Ring Arc 1	BPE	41,760	2		0.2	>5σ detection
Ring Arc 2	BPI	41,470	4		0.2	>5σ detection
Ring Arc 3	BPI	38,430‖	2		0.2	>5σ detection
Ring 2	BPI	38,280‖	1		0.2	>5σ detection
	BPE	38,280‖	1		0.2	>5σ detection

*SS, σ Sagittarii; BP, β Persei; I, ingress; E, egress. †Range values are accurate to ±30 km. ‡Widths are accurate to ±1 km. §Unless otherwise specified, optical depth errors are about ±0.1. ‖Position error is estimated to be ±50 km.

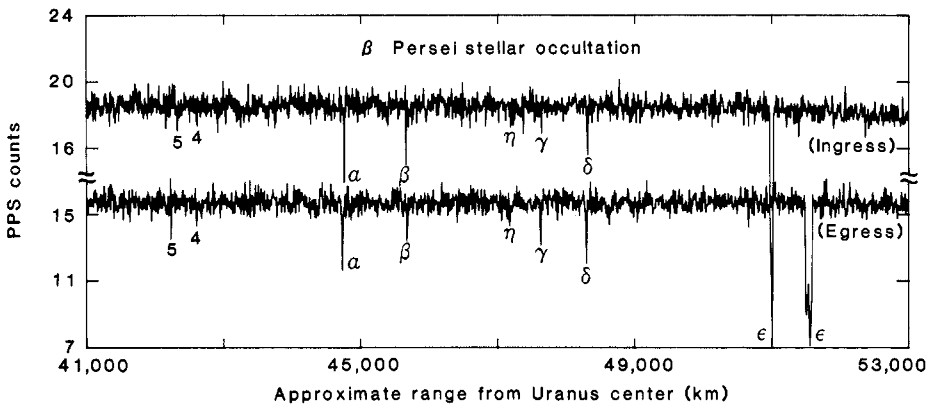

Fig. 8. Compressed overview of the β Persei ring occultation measurements. With the exception of the 6 ring, all the previously known rings that have substantial opacity are easily seen and are labeled with their current names. The 6 ring is the narrowest and least optically thick of the previously known rings, and it is not readily visible at this resolution. The eccentricity of the ε ring is evident. The brightness of the unocculted star (with background light removed) is about 15 counts per 10-msec integration period, and the scattered light from Uranus' atmosphere contributes 0.5 to 3 counts. The data have been binned by 80 points to approximately 10-km resolution.

ring exceeds the value possible for a single layer of particles, the particle centers must be spread in altitude to provide the observed opacity. If we only assume that the particles are spherical and do not assume that there is any particular particle-size distribution, then the largest abundant particles must be three to four times smaller in radius than the vertical extent of the rings; that is, they must have radii of 30 m or less. Additional assumptions can add constraints that lower the limit even further, but these are model-dependent.

Much of the new structure seen in the ε ring is probably caused by satellite perturbations. The resemblance of the features to density-wave peaks is striking (Fig. 7): they are sharp, narrow, extend to an opacity of 2.5 or more, and are separated by broad regions where the opacity is lower. The quasi-periodic structure is also reminiscent of waves. The fit of wave crest position to the density-wave model, however, is not satisfactory for our data and requires more study.

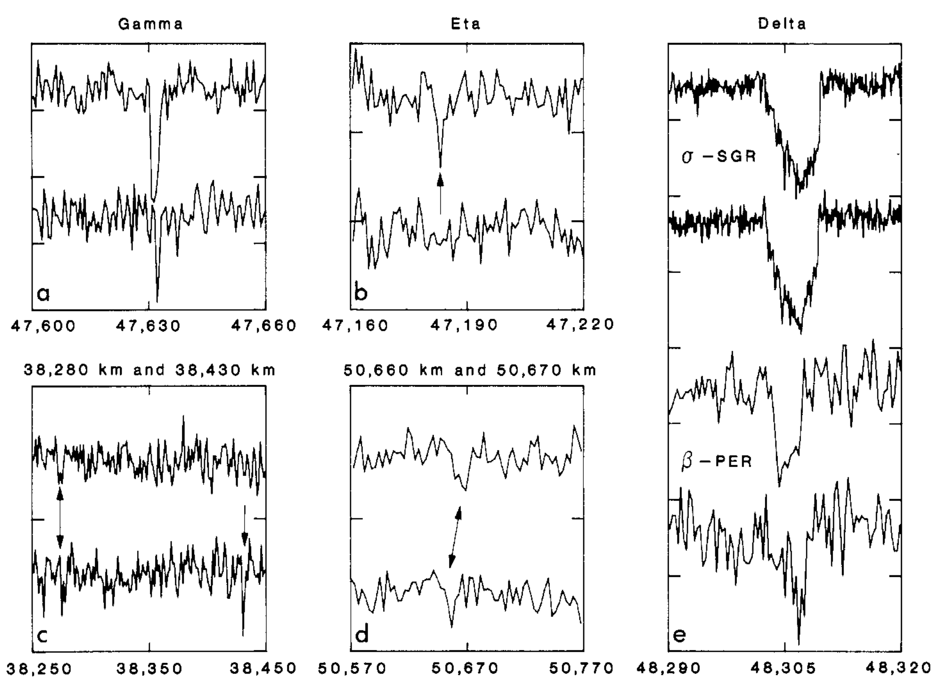

Fig. 9. Composite view of several known rings, two newly discovered rings, and a possible ring arc. For each set of views the ingress cut is the lower trace, and the egress cut is the upper trace. The narrow component of the η ring (b) on the ingress cut was difficult to detect, indicating the possibility of a discontinuous ring. The four cuts of the δ ring that the PPS measured (e) show the changing azimuthal profile. Some of the new structure detected in the rings (c and d) are listed in Table 1. The resolutions vary for each plot set. The raw data were smoothed by boxcar averaging, yielding resolutions of 0.6 km (a), 0.8 km (b), 1.4 km (c), 3.1 km (d), and 0.1 km for σ Sagittarii and 0.4 km for β Persei (e). Tick marks on the vertical axes represent 8 PPS counts.

In addition to the information extracted from the ε ring data, we can state several other conclusions from the data in Table 1 and Figs. 8 and 9.

1) The rings are not azimuthally homogeneous. Even the δ and γ rings, which are nearly circular (*11*), exhibit extremely different spatial distributions of material at the different occultation longitudes measured by the PPS.

2) The narrow component of the η ring, detected and measured at several longitudes by ground-based occultations, is virtually undetectable in the PPS ingress cut for the β Persei occultation at an 80% confidence level on the nondetection. No environmental or instrumental changes occurred during the time period corresponding to the region where the η ring should have been. This narrow component of the η ring may be discontinuous.

3) A large number of narrow, low optical depth, incomplete rings or arcs exist throughout the spatial region sampled by the PPS stellar occultations, including a 3000-km region outside the ε ring. The examples of this class of features (Fig. 9) are each more than 5σ detections, meaning a better than 96% probability that each is real. These features may be similar to the proposed arc-like nature of the Neptunian rings (*12*).

4) The 6 ring, the innermost of the rings detected by ground-based observation, appears to have at least one companion ring arc of equivalent optical depth and width.

Unlike the situation for the Saturn stellar occultation (*1*), the Uranian rings are fully illuminated by sunlight as they occult the star, and some sunlight is scattered by the ring particles into the PPS. The β Persei occultation geometry provides an upper limit on the amount of scattered light observed and hence a limit on the abundance of small particles. Our results show that less than 0.1% of the ε ring's opacity comes from particles smaller than 1 μm (dust). Likewise, if a uniform sheet of dust-like material exists between all pairs of rings, its mean opacity must be 10^{-4} or less.

Our data on the ε ring and data from other Voyager experiments (*6, 9*) suggest the following picture of the Uranian rings. The ring particles are dark and large, and lack dust. Small particles created by collisions are rapidly swept out of the ring system and fall into the planet. Comparing our measured opacity to dynamical estimates for the ring mass (*13*), we find a mean particle size of 20 cm. Physical constraints (*14*) establish the number density of ring particles as 10^{-4} to 10^{-1} m^{-2}; the average separation of particles is 2.5 to 10 times their radius. The variability of ring opacity with longitude and the discovery of partial ring arcs suggest that the Uranian rings are dynamic and perhaps quite young.

Geometric albedos of the satellites and the phase curve of Titania. Disk-integrated brightnesses of the five Uranian satellites were obtained for a range of solar phase angles at two wavelengths (0.27 and 0.75 μm). From these measurements, we determined initial geometric albedos and color ratios for the satellites. For Miranda, Ariel, Umbriel, Titania, and Oberon, respectively, the UV and IR PPS geometric albedos are (UV, IR): 0.27 ± 0.05, 0.30 ± 0.05; 0.27 ± 0.05, 0.31 ± 0.05; 0.14 ± 0.05, 0.15 ± 0.05; 0.17 ± 0.02, 0.24 ± 0.02; and 0.14 ± 0.04, 0.18 ± 0.04. The Uranian satellites have UV:IR color ratios similar to those of the bright icy satellites of Saturn; however, the latter have higher albedos. Figure 10 shows the UV:IR color ratio plotted against the UV geometric albedos of the airless large satellites of Jupiter, Saturn (except Iapetus), and Uranus. Each primary body clearly distinguishes a separate class of satellite surface reflectance properties.

The geometric albedos of the Uranian satellites are not consistent with pure water ice; at least one other low albedo material must also be present. This material must be absorbing at both the UV and IR wavelengths and therefore is not similar to the substance (most likely sulfurous material) that darkens the Galilean satellites, which has low albedo at UV wavelengths and high albedo at IR wavelengths. An additional factor in the Uranian system may be an ice-darkening process caused by magnetospheric particle bombardment.

Another experimental goal was to measure the satellites' phase curves (brightness as a function of the solar phase angle) and opposition surges (the nonlinear increase in brightness at small solar phase angles) (*15, 16*). Figure 11 shows our observations of Titania's opposition surge at 0.75 μm compared with the results from theoretical studies of the effect of mutual shadowing among regolith particles (*15, 16*) for five different compaction states ranging from 25 to 87% void space. The model is most sensitive to observations at phase angles below 6° and suggests a high fraction of void space in Titania's regolith (~85%). Because all of Voyager's observations of Titania were made at solar phase angles greater than 0.8°, they cannot confirm the large opposition surge reported by Earth-based observers (*16*).

The phase coefficient at 0.75 μm for Titania between 4.°5 and 34° is about 0.02 magnitude per degree, a value comparable to the phase coefficients of Dione and Rhea (*17*). In general, bright objects have smaller phase coefficients than dark objects because the increased importance of multiple scattering washes out shadows on their surfaces.

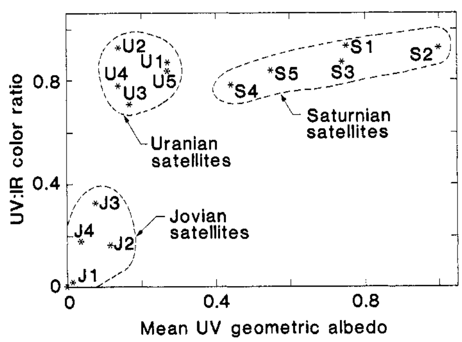

Fig. 10. Color ratio (UV:IR) plotted against UV geometric albedo of planetary satellites. The satellites of Jupiter (*18, 19*) are characterized by a strongly absorbing (most likely sulfurous) material. The Uranian satellites have a surface material that is strongly absorbing in both the UV and the IR. The Saturnian satellites (*17, 20*) most closely approximate the albedo character of pure water-ice [The color ratios for Mimas and Enceladus are for the Voyager ISS UV (0.34 μm) and orange filters (0.59 μm)].

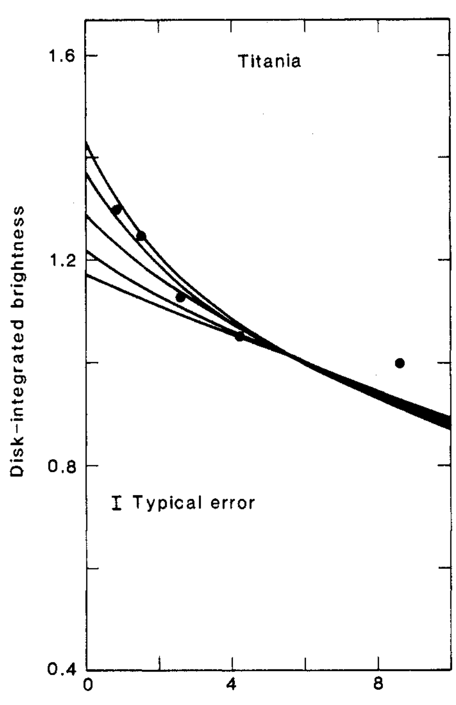

Fig. 11. The disk-integrated phase curve of Titania in the PPS deep red filter (0.75 μm), showing its opposition surge at small phase angles. The theoretical curves are the results from a shadowing model (*16*) for various compaction states of a planetary regolith. The upper curve represents a loosely compacted regolith with 87% void space between particles, and the lowest curve is that expected for a highly compacted surface with only 25% void space. The intermediate curves (top to bottom) represent 83, 75, and 58% void space. The data are normalized at phase angle 6°.

Because Dione and Rhea have higher geometric albedos than Titania (*17*), the value for Titania's phase coefficient is somewhat lower than expected.

Large opposition surges consistent with a loosely packed regolith have also been reported on other bodies in the solar system, such as the Jovian satellite Io (*18*). The mechanisms for creating Io's highly porous surface are different from those at work on Titania. In the former case, the upper surface most probably consists of freshly fallen material from the active volcanoes. In the case of Titania, where no active vulcanism has been observed, the porous regolith is probably due to "gardening" processes caused by constant bombardment of the surface by meteorites over long periods of time. Our initial findings suggest that the regolith texture of Titania is not consistent with recent resurfacing events, such as the outflow of ice slurries on the surface.

REFERENCES AND NOTES

1. A. L. Lane *et al.*, *Science* **215**, 537 (1982).
2. C. W. Hord *et al.*, *ibid.* **206**, 956 (1979); M. G. Tomasko, E. Karkoschka, S. Martinek, *Icarus* **65**, 218 (1986).
3. Acetylene has been detected in the high atmosphere [A. L. Broadfoot *et al.*, *Science* **233**, 74 (1986)], and Atreya and Romani [S. K. Atreya and P. N. Romani, in *Planetary Meteorology*, G. Hunt, Ed. (Cambridge Univ. Press, Cambridge, 1985), pp. 17–68] have argued that photochemically produced acetylene should be abundant enough to condense at temperatures below 70 K; that is, near pressures of a few millibars for current estimates of the temperature structure [J. Appleby, *Icarus* **65**, 383 (1986)]. Acetylene does not absorb sufficiently at 0.27 μm and longer wavelengths to be detected, but acetylene polymers, which have been proposed as possible aerosols on Titan, do [M. Allen, J. P. Pinto, Y. L. Yung, *Astrophys. J.* **242**, L125 (1980)]. Polyacetylene production from gas-phase reactions is slow in the atmospheres of the giant planets and is thought to be negligible compared to N_2H_4 and P_2H_4 production on Jupiter and Saturn [R. A. West, D. F. Strobel, M. G. Tomasko, *Icarus* **65**, 161 (1986)]. Polyacetylene photochemistry, however, may well be the leading candidate for Uranus and Neptune since the partial pressure of ammonia is extremely low in the stratospheres of those planets, and phosphine has not yet been observed. Polyacetylene production may be stimulated by condensed-phase photochemical reactions occurring in UV-irradiated acetylene aerosols.
4. R. A. West *et al.*, *J. Geophys. Res.* **88**, 8699 (1983).
5. J. B. Pollack *et al.*, *Icarus* **65**, 442 (1986).
6. G. L. Tyler *et al.*, *Science* **233**, 79 (1986).
7. L. W. Esposito *et al.*, *J. Geophys. Res.* **88**, 8643 (1983).
8. J. L. Elliot and P. D. Nicholson, in *Planetary Rings*, R. Greenberg and A. Brahic, Eds. (Univ. of Arizona Press, Tucson, 1984), pp. 25–72.
9. B. A. Smith *et al.*, *Science* **233**, 43 (1986).
10. J. N. Cuzzi, *Icarus* **63**, 312 (1985).
11. R. G. French, J. L. Elliot, S. E. Levine, in preparation.
12. W. B. Hubbard *et al.*, *Nature (London)* **319**, 636 (1986).
13. P. Goldreich and S. D. Tremaine, *Astron. J.* **84**, 1638 (1979).
14. The upper limit for the surface number density is derived from the ϵ ring's surface mass density (*13*) combined with the minimum of the particle size derived from the radio occultation differential opacity (*6*). The lower limit is from the PPS-measured optical depth (τ = 0.5 at maximum ϵ ring width; Table 1), and the maximum particle size derived from the PPS upper limit on the ring's vertical thickness (<150 m, which implies a radius <30 m). The particle separation is derived from the measured

optical depth and the range of permissible particle sizes.
15. W. M. Irvine, *J. Geophys. Res.* **71**, 2931 (1966).
16. Theoretical studies, laboratory experiments, and astronomical observations of other objects in the solar system have shown that a determination of the phase curve is important in understanding the physical nature (composition, particle size, and degree of compaction) of a planetary regolith [B. W. Hapke, *Astron. J.* **71**, 333 (1966); J. Veverka, in *Planetary Satellites*, J. Burns, Ed. (Univ. of Arizona Press, Tucson, 1977), pp. 171–209]. Especially important is the opposition surge at small phase angles (<6°). Previous ground-based observations of the Uranian satellites have been limited, of necessity, to solar phase angles of less than 3°.0 [R. H. Brown and D. P. Cruikshank, *Icarus* **55**, 83 (1983)], and therefore the full solar phase angle range of the opposition surge region was unknown before this study. The conventional explanation of the opposition surge is that mutual shadowing among the particles in the optically active portion of the regolith disappears as the face of the object becomes illuminated to the observer. In general, fluffy surfaces exhibit greater opposition surges.
17. B. J. Buratti and J. Veverka, *Icarus* **58**, 254 (1984); B. J. Buratti, *ibid.* **59**, 392 (1984).
18. R. M. Nelson *et al.*, in preparation.
19. R. M. Nelson and B. W. Hapke, *Icarus* **36**, 304 (1978).
20. M. Noland *et al.*, *ibid.* **23**, 334 (1974).
21. We thank the members of the Voyager flight team, who made possible the successful encounter of the PPS with Uranus; P. D. Nicholson and J. Colwell for timing of the predicted occultation events; and M. D. Morrison (JPL) and A. Bahrami (LASP) for exceptional software wizardry. We also thank NASA's Office of Information Systems (code EI) Pilot Planetary Data System Project at the Jet Propulsion Laboratory for computational assistance in the rapid transformation of flight telemetry into scientific results.

31 March 1986; accepted 5 May 1986

Infrared Observations of the Uranian System

R. Hanel, B. Conrath, F. M. Flasar, V. Kunde, W. Maguire, J. Pearl, J. Pirraglia, R. Samuelson, D. Cruikshank, D. Gautier, P. Gierasch, L. Horn, P. Schulte

The infrared interferometer spectrometer (IRIS) on Voyager 2 recorded thermal emission spectra of Uranus between 200 and 400 cm^{-1} and of Miranda and Ariel between 200 and 500 cm^{-1} with a spectral resolution of 4.3 cm^{-1}. Reflected solar radiation was also measured with a single-channel radiometer sensitive in the visible and near infrared. By combining IRIS spectra with radio science results, a mole fraction for atmospheric helium of 0.15 ± 0.05 (mass fraction, 0.26 ± 0.08) is found. Vertical temperature profiles between 60 and 900 millibars were derived from average polar and equatorial spectra. Temperatures averaged over a layer between 400 to 900 millibars show nearly identical values at the poles and near the equator but are 1 or 2 degrees lower at mid-latitudes in both hemispheres. The cooler zone in the southern hemisphere appears darker in reflected sunlight than the adjacent areas. An upper limit for the effective temperature of Uranus is 59.4 kelvins. Temperatures of Miranda and Ariel at the subsolar point are 86 ± 1 and 84 ± 1 kelvins, respectively, implying Bond albedos of 0.24 ± 0.06 and 0.31 ± 0.06, respectively. Estimates of phase integrals suggest that these satellites have unusual surface microstructure.

During the Voyager 2 encounter, Uranus, Miranda, and Ariel were investigated by Voyager's infrared interferometer spectrometer (IRIS), which recorded thermal emission spectra between approximately 200 and 400 cm^{-1} (25 and 50 μm) and reflected solar radiation in the visible and near infrared. IRIS consists of a Michelson interferometer, which covers the thermal spectrum with a resolution of 4.3 cm^{-1}, and a bore-sighted, single-channel radiometer sensitive between 0.4 and 1.5 μm (*1*). Both devices share a 50-cm Cassegrain telescope with a common circular field of view of 0.125° half-cone angle. Absolute calibration of the interferometer is accomplished by scaling the planetary and satellite spectra at each wavenumber interval to deep space spectra and maintaining the instrument at 200 ± 0.1 K. The radiometer is calibrated by occasionally viewing a diffuse reflector exposed to sunlight. IRIS results for the Jovian and Saturnian systems have been summarized (*2*). We now present initial results for Uranus and two of its satellites; we obtained no useful information about the rings.

The brightness spectrum of Uranus. The signal-to-noise ratio (S:N) for an individual Voyager 2 spectrum is greater than 1 between 190 and 320 cm^{-1} and reaches a maximum of about 8 at approximately 230 cm^{-1}. For most purposes we wished to increase this ratio by averaging spectra; the improvement in S:N is proportional to the square root of the number of spectra included in the average. Thus for the averages of south polar and equatorial spectra (Fig. 1), the maximum value of S:N is 195 and 90, respectively.

The thermal spectrum of Uranus is determined by the He abundance, the para-hydrogen fraction, the vertical atmospheric temperature profile, and the properties and vertical distribution of clouds. In principle, all these parameters may be extracted from sufficiently precise spectral measurements, although the solutions are not necessarily unique.

Helium abundance. The atmospheric He abundance can be obtained from the shape of the thermal spectrum or from a comparison of IRIS spectra with RSS data. For both methods, the equatorial spectrum of Fig. 1 (recorded at 5°S, the approximate latitude of the radio occultation points) was used. First, we examined the sensitivity of the spectral shape to various atmospheric parameters. A reference spectrum was calculated for an emission angle of 57°, for a He mole fraction of 0.15, for an equilibrium para-hydrogen fraction, and without the effects of CH_4 gas or clouds. Each parameter was then varied to test the effect on the spectrum. Collision-induced absorption coefficients for H_2–H_2, H_2–He, and H_2–CH_4 were calculated as described (*3*) with the incorporation of recent improvements from laboratory data.

The effect of He abundance variations is shown in Fig. 2. In an atmosphere composed of H_2 and He, an opacity minimum occurs near 200 cm^{-1} as a result of the relative strength of the pressure-induced $S(0)$ transition of H_2 and the translational H_2 opacity, which is strongly affected by collisions of H_2 molecules with He atoms. The position of the resulting brightness temperature maximum depends only weakly on atmospheric temperature but strongly on the He abundance. The broad maximum shifts to higher wavenumbers with increasing He concentration. The position of the maximum also depends strongly on the para-hydrogen fraction (Fig. 3). This fraction is expected to lie between the high-temperature limit or normal value (0.25) and the equilibrium value for the ambient atmospheric temperature. The maximum shifts to higher wavenumbers with decreasing para-hydrogen fraction.

The effect of gaseous CH_4 at the maxi-

R. Hanel, B. Conrath, F. M. Flasar, V. Kunde, W. Maguire, J. Pearl, J. Pirraglia, R. Samuelson, Laboratory for Extraterrestrial Physics, NASA Goddard Space Flight Center, Greenbelt, MD 20771.
D. Cruikshank, Institute of Astronomy, University of Hawaii, Honolulu, HI 96822.
D. Gautier, Paris Observatory, 92190 Meudon, France.
P. Gierasch, Department of Astronomy, Cornell University, Ithaca, NY 14853.
L. Horn and P. Schulte, Jet Propulsion Laboratory, California Institute of Technology, Pasadena, CA 91109.